JCB Journal of Cell Biology

REPORT

ATG2 transports lipids to promote autophagosome biogenesis

Diana P. Valverde[1]*, Shenliang Yu[1]*, Venkata Boggavarapu[2], Nikit Kumar[1], Joshua A. Lees[1], Thomas Walz[2], Karin M. Reinisch[1], and Thomas J. Melia[1]

During macroautophagic stress, autophagosomes can be produced continuously and in high numbers. Many different organelles have been reported as potential donor membranes for this sustained autophagosome growth, but specific machinery to support the delivery of lipid to the growing autophagosome membrane has remained unknown. Here we show that the autophagy protein, ATG2, without a clear function since its discovery over 20 yr ago, is in fact a lipid-transfer protein likely operating at the ER–autophagosome interface. ATG2A can bind tens of glycerophospholipids at once and transfers lipids robustly in vitro. An N-terminal fragment of ATG2A that supports lipid transfer in vitro is both necessary and fully sufficient to rescue blocked autophagosome biogenesis in *ATG2A/ATG2B* KO cells, implying that regulation of lipid homeostasis is the major autophagy-dependent activity of this protein and, by extension, that protein-mediated lipid transfer across contact sites is a principal contributor to autophagosome formation.

Introduction

Large cytoplasmic toxins such as protein aggregates or dysfunctional mitochondria are removed from the cytoplasm through the macroautophagy pathway. This clearance mechanism depends on the de novo formation of a new organelle called the autophagosome that engulfs the toxins and delivers them to the lysosome for degradation. Many different organelles have been implicated as potential sources of membrane supporting autophagosome growth, but the mechanisms of lipid delivery from these organelles to the maturing autophagosome remain uncertain. Vesicle trafficking and subsequent lipid delivery via fusion are widely thought to play a major role in the early membrane remodeling events of autophagosome biogenesis (Molino et al., 2017). However, the close proximity of autophagosomes to other organelles (Zhao et al., 2017, 2018; Gómez-Sánchez et al., 2018) also suggests the intriguing possibility that direct lipid transport may also occur at one or more putative contact sites. Still, no lipid transfer proteins operating at such contact sites were known.

The function of ATG2 proteins has been mysterious ever since their discovery in the seminal autophagy screens of the early 1990s (Tsukada and Ohsumi, 1993; Harding et al., 1995). They are very large (e.g., ATG2A is ∼1,900-aa long) but lack sequence similarity to other proteins, except for short stretches of ∼100 aa at the N and C termini called chorein domains, which are also found within the VPS13 family (Pfisterer et al., 2014a; Muñoz-Braceras et al., 2015). We recently reported that VPS13 functions as a lipid transport protein mediating glycerophospholipid transport between organelles at membrane contact sites (Kumar et al., 2018). The N-terminal sequence it shares with ATG2, known as the chorein_N segment, forms a cap for a larger tubular structure whose hydrophobic cavity solubilizes lipids to transport them between membranes (Fig. 1 A). Here we show that in human ATG2A, the chorein_N sequence indicates the presence of a lipid transfer domain. Further, our imaging suggests localization of human ATG2A to contact sites between the ER and the autophagophore, as might be expected for a function in lipid transfer between these organelles. We also demonstrate that a small N-terminal fragment, which is similar to the structurally characterized fragment of VPS13 and which supports lipid transfer in vitro, can fully substitute for the full-length ATG2A in vivo. Together, these data support a key role for nonvesicular lipid transfer, mediated by ATG2, during the early stages of autophagosome formation.

Results and discussion

ATG2A can bind tens of lipids

To determine whether ATG2 proteins might solubilize lipids, a prerequisite for a lipid transport function, we overexpressed human ATG2A in mammalian cells (Expi293F), isolated it via an

[1]Department of Cell Biology, Yale University School of Medicine, New Haven, CT; [2]Laboratory of Molecular Electron Microscopy, The Rockefeller University, New York, NY.

*D.P. Valverde and S. Yu contributed equally to this paper and the first author was selected by a coin flip; Correspondence to Thomas J. Melia: thomas.melia@yale.edu; Karin M. Reinisch: karin.reinisch@yale.edu.

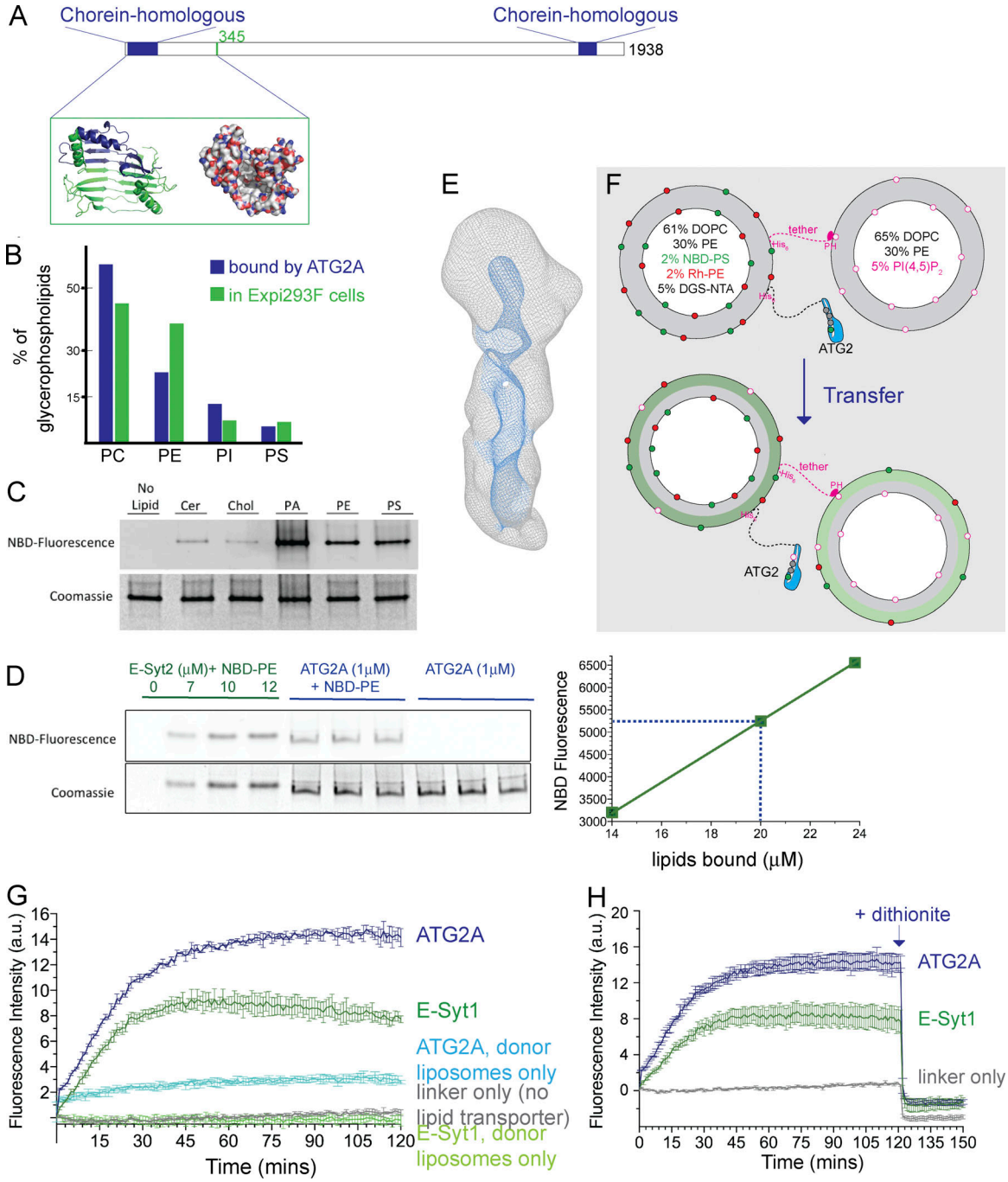

Figure 1. **ATG2A binds and transfers glycerophospholipids between membranes. (A)** ATG2 architecture. Sequences homologous to VPS13 proteins are indicated. Inset shows a fragment from the ATG2A N terminus modeled on the crystal structure of Vps13 (PDBID 6CBC). The chorein_N sequence is indicated in blue. A space-filling model colored according to atom type (red for oxygen, blue for nitrogen, and white for carbon) suggests that a cavity in this fragment is hydrophobic and suitable for solubilizing glycerophospholipid fatty acid chains. **(B)** Lipids that copurified with ATG2A from Expi293 cells according to abundance. No sterols, diglycerides, or triglycerides were detected. Relative abundance of glycerophospholipids in Expi293 cells is indicated (Lees et al., 2017). **(C)** ATG2A was incubated with NBD-tagged lipids and examined by native PAGE. Phospholipids, visualized by their fluorescence, comigrated with protein, visualized by Coomassie blue staining. Cer, ceramide; Chol, cholesterol; PA, phosphatidic acid. **(D)** A native gel assay was used to compare NBD fluorescence associated with ATG2A and indicated quantities of the extended-synaptotagmin2 (E-Syt2) SMP domain, known to accommodate two glycerophospholipids within its cavity (Schauder et al., 2014). Based on this comparison, each ATG2A binds to ~20 lipid molecules. The experiment was performed in triplicate. SD is shown. **(E)** The 3D cryo-EM reconstruction of ATG2A at a nominal resolution of ~15 Å, shown in mesh representation (6.5 signal/noise). A cavity (or cavities) highlighted blue runs along the length of ATG2A. Fig. S1 shows additional views of ATG2A. **(F)** In the transfer assay, donor and acceptor liposomes (compositions indicated) were tethered together in the presence or absence ATG2A linked to the donor liposomes. The assay monitors the increase in NBD-PS fluorescence after lipid transfer from donor liposomes, where NBD fluorescence is quenched via FRET with Rh-PE, to acceptor liposomes. **(G)** The fluorescence increase observed is consistent with lipid transfer at a rate similar to the lipid transfer domain of extended-synaptotagmin1 (E-Syt1), a previously validated lipid transporter (Saheki et al., 2016; Yu et al., 2016; Bian et al., 2018), tethered analogously to ATG2A. The fluorescence increase is much smaller when only donor

but not acceptor liposomes are present. The small but still significant increase under these conditions is most likely due to lipid extraction by the transport proteins and would not be expected in the case of fusion or hemifusion between donor liposomes. The increase in this case is larger for ATG2A than E-Syt1, likely reflecting that the ATG2A cavity accommodates more lipids. All experiments were performed in triplicate. SD is shown. **(H)** Addition of dithionite reduces the NBD fluorescence equally for ATG2A, E-Syt1, or the tether-only control, indicating that membrane fusion has not occurred. Each experiment was performed in triplicate; SDs are shown.

N-terminal FLAG tag and size-exclusion chromatography, and analyzed by liquid chromatography/tandem mass spectrometry lipids that copurify with it. Despite the size-exclusion chromatography step, which removes weakly bound lipids (Maeda et al., 2013), multiple glycerolipids (>>10) were associated with each protein molecule, similar to VPS13 (Kumar et al., 2018). ATG2A copurified almost exclusively with glycerophospholipids, which were bound nonspecifically according to their cellular abundance, and not other classes of lipids (Fig. 1 B). Further supporting that ATG2A can solubilize lipids, it comigrates with nitrobenzoxadiazole (NBD)-labeled glycerophospholipids as assessed by native gel (Fig. 1 C). For confirmation that ATG2A binds to glycerophospholipids in bulk, we used the native gel assay to compare NBD fluorescence associated with ATG2A and an equimolar quantity of the Extended-Synaptotagmin2 SMP domain, a well-characterized lipid transport module that accommodates two lipids (including NBD-labeled lipids) within its hydrophobic cavity (Schauder et al., 2014). Based on this comparison, each ATG2A binds to ∼20 lipid molecules (Fig. 1 D).

A 3D single particle reconstruction of ATG2A, obtained by cryo-EM at ∼15-Å nominal resolution, reveals a ∼16-nm-long club-shaped molecule, consistent with reports based on negative-stain EM (Zheng et al., 2017a; Chowdhury et al., 2018; Figs. 1 E and S1). Intriguingly, the cryo-EM reconstruction further shows an extended cavity, or a series of cavities, along the length of ATG2A. The diameter of the cavity is ∼20 Å, matching well the cavity diameter in a crystallized fragment of the VPS13 lipid transport structure. Thus, the cavity is large enough to accommodate multiple glycerophospholipids at once, and we propose that, lined with hydrophobic residues, it could solubilize lipids and function in their transport.

ATG2A transports lipids in vitro

We next used a fluorescence resonance energy transfer (FRET)–based assay to interrogate whether ATG2A can transfer lipids between membranes (Fig. 1 F). We mixed donor liposomes containing DGS-NTA, NBD-phosphatidylserine (NBD-PS), and Rhodamine-phosphatidylethanolamine (Rh-PE) with acceptor liposomes containing phosphatidylinositol 4,5-bisphosphate ($PI(4,5)P_2$) and lacking the fluorescent lipids, then added ATG2A, which was tethered to donor liposomes via a C-terminal hexahistidine tag and a linker construct. The linker construct comprises an N-terminal hexahistidine tag, which interacts with DGS-NTA in the donor liposomes, and a C-terminal pleckstrin homology domain, which interacts with phosphoinositides in the acceptor liposomes. Thus, the linker tethers together donor and acceptor liposomes to mimic the architecture of membrane contact sites, where ATG2A likely functions (see below). Initially, FRET between NBD and Rh in the donor liposomes quenches NBD fluorescence. Transfer of NBD-PS, Rh-PE, or both to acceptor liposomes would result in their dilution, decreased FRET, and an increase in NBD fluorescence. Consistent with ATG2A-mediated lipid transfer, we observed an increase in NBD fluorescence upon addition of proteins (but not the linker construct alone; Fig. 1 G). The NBD fluorescence of reactions with and without ATG2A were the same following the further addition of dithionite (Meers et al., 2000), which quenches NBD fluorescence only in the outer leaflet of the liposome bilayer but does not affect the inner leaflet, ruling out that the ATG2A-mediated fluorescence increase is due to fusion between donor and acceptor liposomes (Fig. 1 H). We observed a smaller increase in NBD fluorescence in reactions with ATG2A lacking acceptor liposomes, corresponding to a scenario in which ATG2A extracts fluorescent lipids from the donor liposomes but cannot deliver them to acceptor liposomes. For a positive control, we performed the same FRET-based assay, but with the SMP module of the previously characterized glycerophospholipid transporter E-Syt1 replacing ATG2A (Saheki et al., 2016; Yu et al., 2016). The efficiency of ATG2A-mediated fluorescent lipid transfer was similar to that of E-Syt1, making it plausible that ATG2A might function as a glycerophospholipid transporter in vivo.

Although sequence conservation between VPS13 and ATG2 falls off after the chorein_N sequence, similarity in their secondary structure persists. To confirm that the structural similarity between ATG2A and VPS13 extends beyond the chorein_N sequence, we made a minimal version of ATG2A comprising only its 345 N-terminal residues, which corresponds closely to the crystallized fragment of the VPS13 lipid transport structure (Fig. 1 A, inset). As expected if the chorein_N sequence caps a similar lipid transfer fold in ATG2A and VPS13, mini-ATG2A is soluble and transfers lipids in the FRET-based assay (Fig. 2, A and B). This lipid transfer ability is abrogated in two mutant forms of mini-ATG2A in which clusters of hydrophobic residues lining the presumed lipid binding cavity are changed to charged amino acids (Fig. 2, C and D), making the cavity more hydrophilic and unsuitable for lipid binding.

Lipid transport by mini-ATG2A is sufficient to drive macroautophagy

Ideally, to evaluate the biological relevance of the ATG2 lipid transfer ability observed in vitro, we would test whether a mutant version lacking this ability can substitute for the WT protein in cells. In practice, however, because the lipid-binding cavity of intact ATG2A is massive (we estimate it as four times larger than that of mini-ATG2A) and, moreover, because an atomic resolution model for the intact protein is not available, designing such a mutant is not feasible. We next reasoned that if a major function of ATG2A is in the transfer of lipids, then mini-ATG2A, which is competent for lipid transfer in vitro, might

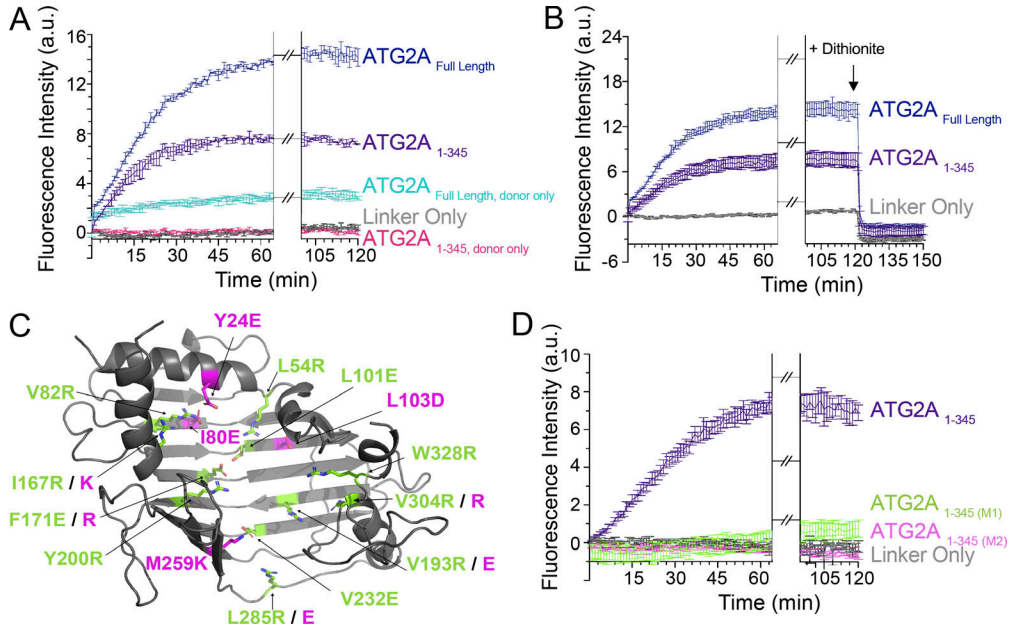

Figure 2. **The N-terminal module in ATG2A transfers lipids in vitro. (A)** FRET-based lipid transfer assay (as in Fig. 1 G) comparing transfer or lipid extraction only (no acceptor liposomes) by full-length and mini-ATG2A. The higher plateaus for full-length ATG2A likely reflect a more extensive cavity accommodating more lipids. **(B)** The dithionite assay (as in Fig. 1 H) rules out that the increases in NBD fluorescence are due to liposome fusion. **(C)** In two mutant forms of mini-ATG2 (M1 and M2), the hydrophobic cleft was made hydrophilic by the inclusion of charged amino acids, indicated in green and purple, respectively, on the structural model. **(D)** Both mutants lose the capacity to transfer lipids in the FRET-based assay. Each experiment was performed in triplicate; SDs are shown.

substitute for the intact protein in vivo, whereas the transfer-incompetent mini-ATG2 mutants would not.

To test the sufficiency of mini-ATG2A, we first generated *ATG2A/ATG2B* double knockout (*ATG2* DKO) human embryonic kidney 293 (HEK293) cells by CRISPR/Cas9. Consistent with previous reports, *ATG2* DKO cells are incapable of completing autophagy (Figs. 3 A and S2; Velikkakath et al., 2012; Tamura et al., 2017; Tang et al., 2017). In the DKO cells, autophagosome-associated proteins including LC3B-II, GL1, and p62 accumulate under full media conditions (Figs. 3 A and S2). Furthermore, LC3B-II fails to undergo autophagy flux, because the levels of this protein do not change when lysosomal degradation is inhibited with bafilomycin A1. Instead, LC3B accumulates at abnormally large immunofluorescent structures (Fig. S2 C). These structures are not mature closed autophagosomes, because both LC3B-II and p62 remain protease sensitive when membranes are isolated by differential centrifugation approaches and subjected to proteinase K exposure (Fig. 3, D and E; Velikkakath et al., 2012). Stable expression of GFP-ATG2A by viral transduction (Fig. 3, A and C–E; and Fig. S2) reverses each of these phenotypes.

Remarkably, expression of a GFP-tagged mini-ATG2A (GFP-ATG2A$_{1–345}$) in DKO cells is also sufficient to rescue each of the autophagy phenotypes (Fig. 3, A and C–E; and Fig. S2). A near-complete rescue is observed when GFP-mini-ATG2A is expressed at levels 10 times endogenous ATG2A, while expression at approximately endogenous levels (off a weaker promoter [PGK]) yields a partial reversal of each phenotype (Fig. S2, E–I). In contrast, the hydrophobic surface mutants that are inactive for lipid transport in vitro are also unable to rescue autophagy, despite expression levels 3–6 times that of the endogenous protein (Fig. 3 B and Fig. S2, I and J).

Other ATG2A constructs did not have the ability to rescue. Expression of a fragment that comprises only the Chorein_N sequence (ATG2A$_{1–139}$) did not restore autophagic function; nor did expression of a mini-ATG2A construct lacking the Chorein_N sequence (ATG2A$_{150–345}$; Fig. S2 K) or a deletion construct lacking only the mini-ATG2A module (Δ1–345; Fig. 3, A and C–E; and Fig. S2). As we did not characterize these other fragments in vitro, we cannot exclude that one or more of them were misfolded. Finally, expression of other glycerophospholipid transport modules, such as the E-Syt2 SMP domain, did not reverse the autophagy phenotypes (Fig. S2 K).

Our finding that the N-terminal mini-module is both required and sufficient to complete ATG2 function in autophagy was unanticipated, as the prevailing view has been that the ability of ATG2 to tether membranes is critical for function in vivo, yet mini-ATG2 (aa 1–345) is unlikely to be capable of the kinds of membrane tethering that were speculated. Mammalian ATG2A has been shown to be capable of membrane tethering in vitro (Chowdhury et al., 2018) via sequences at both its N terminus and via its C-terminal WIPI binding sites. Yeast Atg2 has been suggested to tether in cells, again dependent on the WIPI binding site (Kotani et al., 2018), and to work with Atg9 to coordinate ER–phagophore contact sites, dependent on an Atg9 binding site in the C-terminal half of Atg2 (aa 1,232–1,268; Gómez-Sánchez et al., 2018). In addition, mammalian ATG2 proteins can also target lipid droplets (LDs) via both an amphipathic helix (aa 1,723–1,829; Velikkakath et al., 2012) and an additional short motif (aa 1,830–1,938; Tamura et al., 2017).

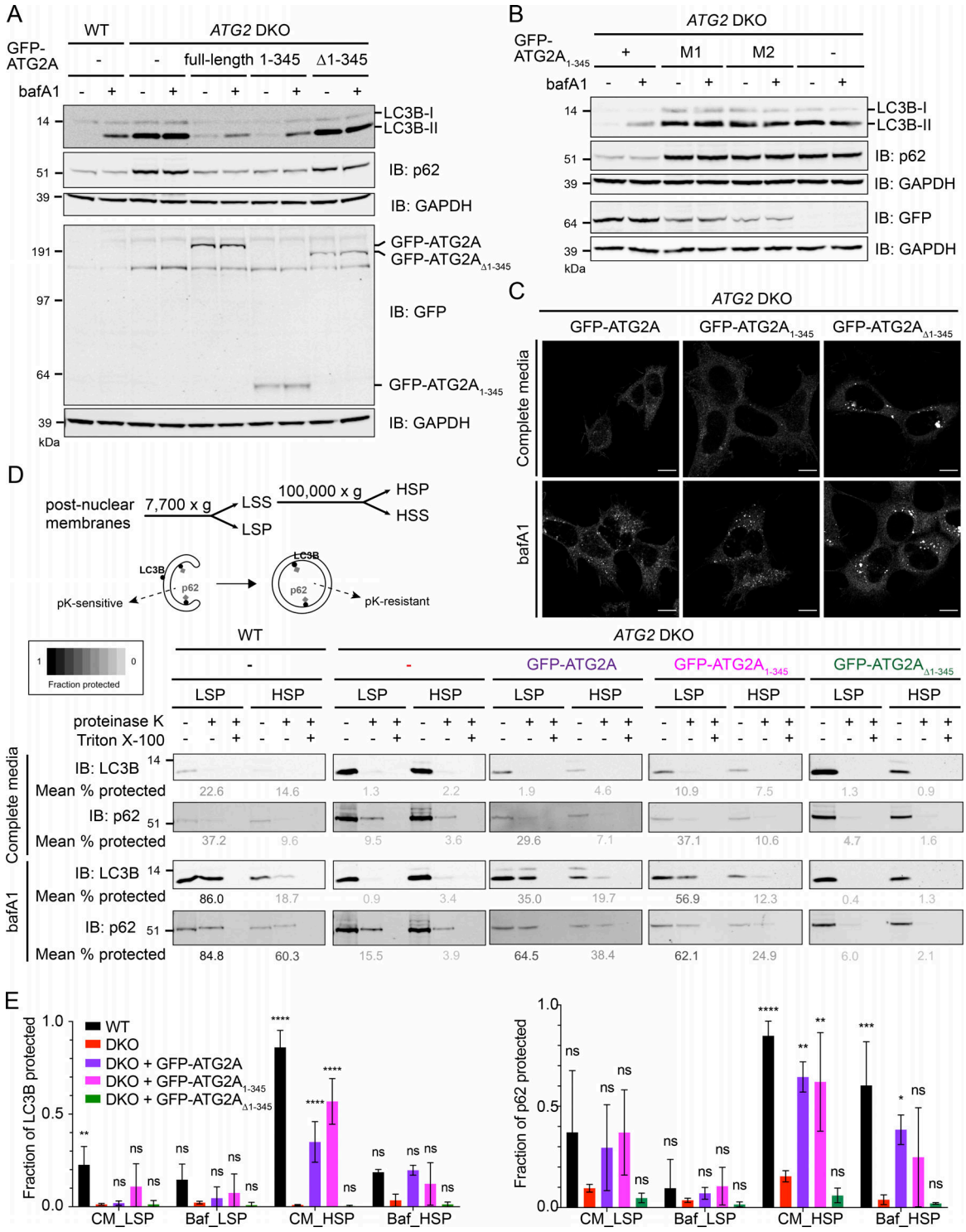

Figure 3. **The N-terminal module in ATG2A is both required and sufficient for autophagosome maturation in *ATG2* DKO cells. (A)** Immunoblots (IB) of WT, *ATG2* DKO, and DKO cells stably expressing full-length GFP-ATG2A, GFP-ATG2A$_{1–345}$, or GFP-ATG2A$_{Δ1–345}$, grown in complete medium ± bafA1. Normal autophagy flux is indicated by the increase in LC3B-II when lysosomes are poisoned with bafA1 (WT, full-length rescue and 1–345 rescue). Likewise, p62 levels are low in autophagy-competent cells. Flux is blocked in the DKO cells or cells rescued with Δ1–345. Quantification of autophagy rescues are shown in Fig. S2 F. GAPDH is a loading control. **(B)** Immunoblots of ATG2 DKO cells rescued with the minifragment or either of the two mutant clusters described in Fig. 2. Quantification of p62 levels is shown in Fig. S2 J. **(C)** Anti-LC3B IF images of DKO cells stably expressing GFP-ATG2A constructs in A and grown in complete medium or complete medium with bafA1. Cells lacking a functional ATG2A (GFP-ATG2A$_{Δ1–345}$), accumulate large LC3-positive structures, while expression of functional ATG2 (GFP-ATG2A and GFP-ATG2A$_{1–345}$) leads to WT-like small puncta that accumulate under bafA1 treatment. Scale bars: 10 µm. **(D)** Postnuclear membranes from indicated cell lines grown in complete medium were differentially centrifuged to generate LSP and HSP fractions. Each fraction was treated with proteinase K, with and without Triton X-100, and subjected to anti-LC3B and anti-p62 immunoblotting. Percentage of protected LC3B or p62 was calculated from the ratio of signal in the proteinase K–treated lane over the nontreated control. Cells with functional ATG2A accumulate proteinase-K resistant

LC3B and p62, particularly in the LSP (WT, GFP-ATG2A, GFP-ATG2A$_{1–345}$), while autophagy-impaired cells (DKO and GFP-ATG2A$_{\Delta1–345}$) do not. The mean value of three independent experiments is shown below. **(E)** Full quantification of p62 and LC3-II levels from experiments in D. Statistical significance was calculated by two-way ANOVA. *, P < 0.05; **, P < 0.01; ***, P < 0.001; ****, P < 0.0001. Expression levels of all GFP-ATG2A constructs is shown in Fig. S2 I. ns, not significant.

Critically, all of these key organelle-targeting motifs, save the isolation membrane-directed N terminus (aa 1–198; Tamura et al., 2017), which must act in concert with another motif for tethering, are in the >80% of the protein not present in mini-ATG2A. The ability of mini-ATG2A, and only the lipid transport–competent version thereof, to rescue autophagy strongly indicates that a main function of this protein is in lipid transport. It is likely that the N-terminal targeting sequence present in mini-ATG2 (Tamura et al., 2017) is important for productive localization. Nevertheless, bidentate interactions with two organelles simultaneously by the full-length ATG2 may enhance its lipid transport efficiency. Indeed, many lipid transport proteins are also tethers whose tethering ability is important for full function in vivo.

ATG2A is localized to autophagosome–ER contact sites

In mammals, autophagosome biogenesis predominantly occurs in association with ER subdomains termed omegasomes (Axe et al., 2008). As such, the proteins that function in early mammalian autophagosome biogenesis have been shown to colocalize with the ER-associated phosphatidylinositol 3-phosphate marker, double-FYVE–containing protein (including GFP-tagged ATG2A; Pfisterer et al., 2014b), but the small size of mammalian autophagosomes has generally precluded distinguishing which of these proteins are simply targeting the autophagosome from those that are restricted to the ER–autophagosome interface where lipid exchange might occur. Furthermore, autophagosomes engage a variety of organelles during biogenesis and are proposed to rely on these organelles to support autophagosome growth. Thus, we sought to rigorously establish at which (if any) autophagosome–organelle interface ATG2A resides during mammalian autophagosome formation.

To establish specific targeting to the contact site, we attempted to follow the continuous labeling of the ER adjacent to the organelle of interest over time, as the two organelles move about in space. This approach requires the protein of interest to be genetically tagged with a live-imaging competent fluorophore. To that end, previous studies have shown that the overexpression of GFP-ATG2A leads to strong labeling of LDs and modest but detectable labeling of autophagic membranes (Velikkakath et al., 2012; Pfisterer et al., 2014b). Indeed, GFP-ATG2A expressed in our DKO cells decorates large circular LDs (made large by the treatment of the cells with oleic acid [OA]; Figs. 4 A and S3), as well as smaller puncta that are positive for the early autophagosome marker WIPI2 (Fig. 4 A, left). Importantly, the small, WIPI2-positive GFP-ATG2A puncta are also uniformly associated with the ER (Fig. 4 B).

To establish the precise localization of full-length ATG2A, we used three-color live imaging of the ER (RFP-Sec61), the autophagosome (BFP-LC3B), and GFP-ATG2A. In rescue experiments in our DKO HEK293 cell line, GFP-ATG2A decorates two structures: (1) large circular structures that are BFP-LC3B negative and presumably are LDs and (2) small stretches of ER that are in direct association with BFP-LC3 puncta (Figs. 4 C and S3 B). This second autophagosome-directed pool remains associated with the ER even throughout the random fluctuations of ER dynamics, continuously demarcating a site of organelle contact with the immediately adjacent or partially overlapping BFP-LC3B (Fig. S3 B). Only a fraction of the ATG2 puncta are also LC3 positive, and only those doubly labeled puncta that reside on relatively sparse regions of the ER can be positively identified as residing between the two organelles. Importantly, similar results were observed following expression of GFP-ATG2A in WT Cos-7 cells, where continuous ER association was apparent throughout the residence time of GFP-ATG2A at forming autophagosomes (Figs. 4 D and S3 C). Thus, we conclude that ER–autophagosome contact sites are likely the primary location of ATG2A function.

These results with GFP-tagged ATG2 proteins do not preclude a role for LDs. Deletion of the minimodule that is necessary to support autophagy and that includes the previously identified autophagosome targeting sequence (Tamura et al., 2017) eliminates colocalization with the WIPI2 structures (structures that accumulate to large sizes in the DKO), but LDs continue to be strongly decorated (Fig. 4 A, right), consistent with earlier work placing LD targeting motifs in the C-terminal half of the protein (Tamura et al., 2017). As membrane targeting of the fully sufficient minimodule alone is not detectable under our expression conditions (Fig. 4 A, middle), we cannot speculate whether GFP-ATG2A must engage LDs to function. Thus, we next attempted to image endogenous ATG2A directly (Fig. 4, E and F). Although a commercially available antibody was not initially effective in immunofluorescence (IF), we could improve its specificity for ATG2A by preclearing the antibody against fixed and perforated cellular material prepared from our DKO cells (Fig. S3, D–G). This cleared antibody selectively recognized ATG2 associated with WIPI2 puncta in WT HEK293 cells but did not label LDs, nor did it detect any structures in the DKO cells (Fig. 4 E and Fig. S3, F and G). In Cos-7 cells, this antibody recognized small puncta, which were also WIPI2 positive and which were again found on the ER (Fig. 4 F). Thus, across multiple cell lines, our imaging results imply that ATG2A localization is at ER–autophagosome contact sites and suggest a role for lipid transfer between these two organelles.

While our imaging data are most consistent with ATG2 operating at the interface between the ER and the isolation membrane, ATG9 vesicles are also thought to target this region (Gómez-Sánchez et al., 2018), and ER–mitochondrial contact sites have also been proposed to play a role in autophagosome biogenesis (Hamasaki et al., 2013). Thus, an absolute identification of the relevant membrane interface will have to await the identification of protein molecules that capture ATG2 on each putative interacting membrane.

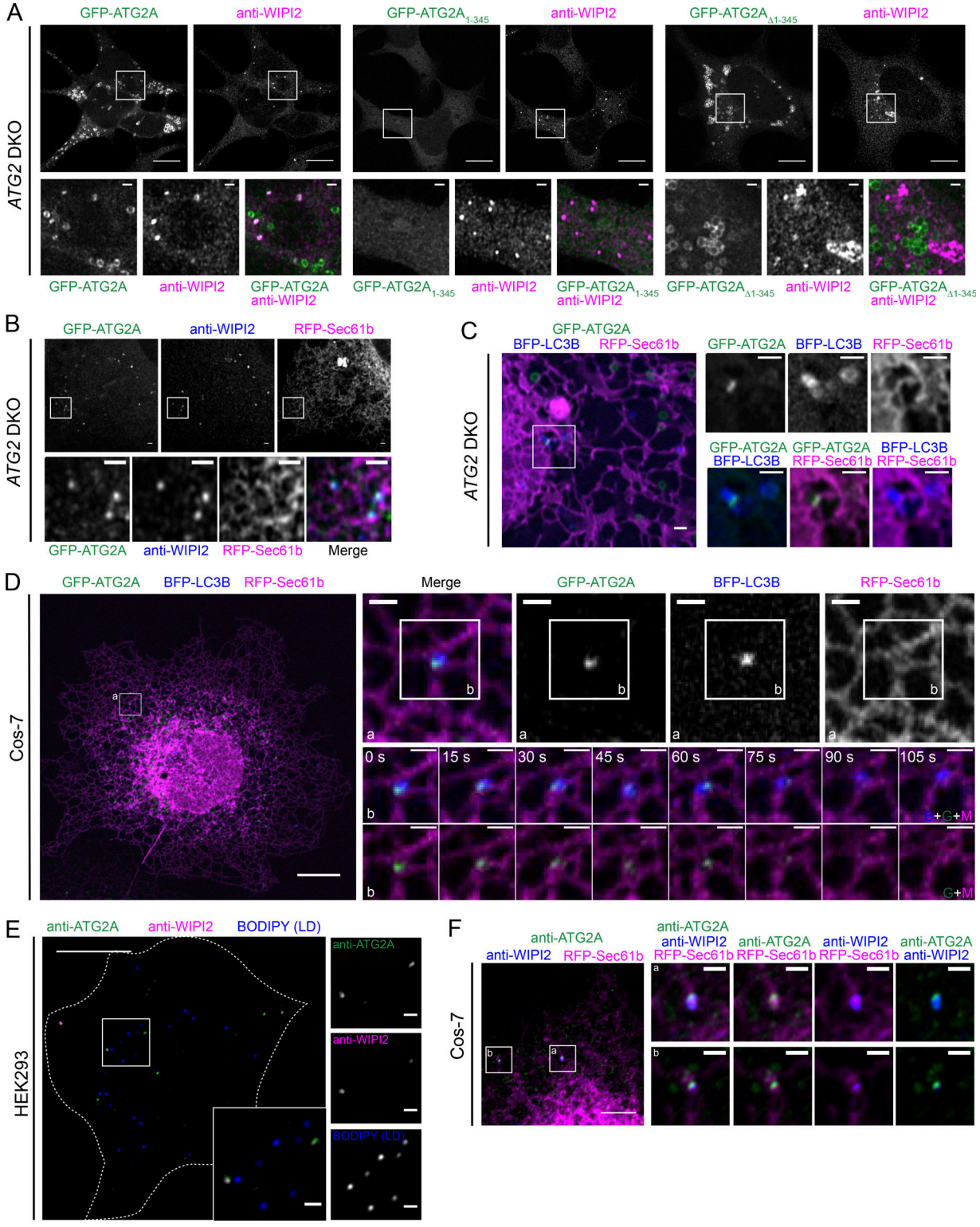

Figure 4. **Overexpressed GFP-ATG2A and endogenous ATG2A localizes at ER–autophagosomal membrane contact sites. (A)** *ATG2* DKO HEK293 cells stably expressing the indicated GFP-ATG2A construct were treated with OA to enlarge LDs, and then incubated in starvation medium (Earle's balanced salt solution) and subjected to anti-WIPI2 IF. Greater than 88% of all WIPI2 positive structures are also GFP-ATG2A positive. Targeting to autophagosomes (WIPI2 structures) is lost with removal of the mini-ATG2 sequence (GFP-ATG2A$_{\Delta 1-345}$). Scale bars: 10 µm; zoomed field: 1 µm. **(B)** GFP-ATG2A localized with early autophagosome markers is also associated with the ER. Anti-WIPI2 IF confocal images in starved *ATG2* DKO cells stably expressing GFP-ATG2A and transiently expressing RFP-Sec61b. Scale bars: 1 µm. **(C)** The late autophagosome marker LC3B colocalized with GFP-ATG2A ∼13% of the time, and these LC3B/GFP-ATG2-positive puncta consistently also associated with the ER. Live imaging of starved *ATG2* DKO cells stably expressing GFP-ATG2A, transiently expressing RFP-Sec61b and BFP-LC3B, and incubated with OA. Note that ring-like GFP-ATG2 structures are likely LDs, are not LC3B-positive, and are not restricted to the ER. Full time course in Fig. S3 B indicates GFP-ATG2A remains directly associated with the ER during the entire time it localizes to the autophagosome. Scale

bars: 1 µm. **(D)** Time-lapse imaging of starved Cos-7 cells stably expressing GFP-ATG2A and transiently expressing RFP-Sec61b and BFP-LC3B. ER localization of autophagosome-associated GFP-ATG2A is similar in WT Cos-7 cells as in DKO HEK293 cells, and again persists throughout the residence time of GFP-ATG2A at LC3B-positive structures. A second longer video example is shown in Fig. S3 C. Scale bars: 10 µm; zoomed field: 1 µm. **(E)** Endogenous ATG2A is localized only on autophagosomes (WIPI2-positive) and not LDs. Commercially available ATG2A antibodies were precleared with *ATG2* DKO cellular material to improve signal to noise (Fig. S3). Then, starved HEK293 cells were treated with OA, labeled with BODIPY 558/568, and subjected to anti-WIPI2 and precleared anti-ATG2A IF. Scale bars: 10 µm; zoomed field: 1 µm. **(F)** Endogenous ATG2A is associated with autophagosome markers and the ER. Starved Cos-7 cells were transiently transfected with RFP-Sec61b, treated with OA, and subjected to anti-WIPI2 and precleared anti-ATG2A IF. Scale bars: 5 µm; zoomed field: 1 µm. For all panels, representative confocal images from at least three independent experiments are shown.

Our results strongly imply that a principal role for ATG2A during autophagy is to maintain lipid homeostasis on growing autophagosomes in support of the organelle's growth and closure through lipid transfer activity at ER-isolation membrane contact sites. Although details of early autophagophore formation are currently thought to differ in higher and lower eukaryotes (Hurley and Young, 2017), the finding that yeast Atg2 concentrates on expanded phagophores near the ER (Suzuki et al., 2013; Gómez-Sánchez et al., 2018) implies that the lipid-transfer mechanism we describe here is likely conserved. The chorein domain–containing family of lipid transfer proteins, which now includes ATG2 and VPS13 proteins, are distinguished from other lipid-transfer families by their capacity to bind and likely transfer tens of glycerolipids at once. This dramatic delivery might be used to rapidly drive an equilibration of the lipid composition between the isolation membrane and the ER, providing a possible mechanism to maintain high surface densities of high-demand glycerophospholipids on the autophagosome, such as phosphatidylethanolamine. An alternative intriguing possibility is that the bulk delivery of lipid could be used to directly support the growth of the isolation membrane, provided the delivery mechanism could be harnessed to be unidirectional. Such a mechanism would be independent of or possibly complementary to vesicle-mediated delivery of membrane, and would be consistent with isolation membrane growth that occurs predominantly before the membrane is associated with SNARE-related membrane fusion machinery.

Materials and methods

Plasmids and reagents

For protein expression constructs, the coding sequence of human ATG2A was PCR amplified from pEGFP-C1-hATG2A from N. Mizushima (University of Tokyo, Tokyo, Japan; Addgene; 36456) and subcloned into p3xFLAG-CMV-10 with the FLAG tag at the N terminus. $ATG2A_{FL\ Tether}$ additionally incorporates a C-terminal 31 residue linker ($(Gly_4Ser)_5$-His_6); the construct corresponding to mini-ATG2A was made from $ATG2A_{FL\ Tether}$ by deleting residues 346–1,938 using Q5 site-directed mutagenesis (NEB). In each of the mutated forms of mini-ATG2A, multiple hydrophobic residues in the cavity were replaced by charged residues (mutant 1: L54R, V82R, L101E, I167R, F171E, V193R, Y200R, V232E, L285R, V304R, and W328R; mutant 2: Y24E, I80E, L103D, I167K, F171R, V193E, M259K, L285E, and V304R). Coding sequences for the mutant forms of mini-ATG2 were purchased from Genscript and replaced the WT sequence in the mini-ATG2 construct. The SMP domain of E-Syt1 (93–327) and a tether-only construct, consisting of the hexahistidine-tagged pleckstrin homology domain of rat PLCδ (11–140), were gifts from X. Bian and P. De Camilli (Yale University, New Haven, CT; described in Bian et al. [2018]). The expression plasmid for human E-Syt2 (residues 163–634) was previously described (Schauder et al., 2014).

GFP-ATG2A, GFP-$ATG2A_{1–345}$, GFP-$ATG2A_{Δ1–345}$, and BFP-LC3B for use in cell experiments were generated by Gibson assembly of three fragments: digested backbone pLVX-puro (Clontech; 632159) or pLenti-III-PGK (Abm), gel-purified PCR products of GFP/BFP-10xGS linker, and 10xGS linker-insert. ATG2A variants were PCR amplified using the template pEGFP-C1-hATG2A (Addgene; 36456). RFP-Sec61b was a kind gift from T. Rapport (Harvard University, Cambridge, MA). Bafilomycin A1 was purchased from Enzo (BML-CM110-0100).

All EM reagents were purchased from Electron Microscopy Sciences. Lipids were purchased from Avanti Polar Lipids: DOPC (850357), NBD-PE (810144), NBD-PS (810198), NBD–phosphatidic acid (810138), NBD-ceramide (810211), Rh-PE (810150), DGS-NTA (Ni; 790404), $PI(4,5)P_2$ (840046), liver PE (840026), and NBD-cholesterol (810252). Antibodies used for immunoblotting in this study include anti-LC3B (rabbit; CST; 3868S), anti-GABARAPL1 (rabbit; CST; 26632), anti-GFP (rabbit; CST; 2956S), anti-ATG2A (rabbit; CST; 15011S), anti-ATG2B (rabbit; Sigma; HPA019665), anti-p62 (mouse; BD Biosciences; 610833), and anti-GAPDH (mouse; Thermo Fisher Scientific; MA5-15738). Primary antibodies used for IF include anti-FLAG (mouse; Sigma; F1804; 1:500 dilution), anti-WIPI2, clone 2A2 (mouse; Millipore; MABC91; 1:250), anti-ATG2A (rabbit; 1:100), and anti-LC3B (rabbit; MBL; PM036; 1:500). Secondary antibodies used for IF include anti-rabbit secondary antibody conjugated with Alexa Fluor 488 and 594 (Thermo Fisher Scientific; A11034, A11008, A11037, or R37117; 1:500) and anti-mouse secondary antibody conjugated with Alexa Fluor 488 (Thermo Fisher Scientific; A32723; 1:500).

Protein expression and purification

To express 3xFLAG ATG2A constructs for in vitro studies, Expi293 cells (Invitrogen) were transiently transfected according to the manufacturer's instruction (Longo et al., 2013; Fang et al., 2017). Protein expression was enhanced by addition of nonessential amino acids and valproic acid (3.5 mM final concentration) 18 h after transfection. Cells were harvested by centrifugation 65 h after transfection, resuspended in lysis buffer (50 mM Hepes, pH 8.0, 500 mM NaCl, 1 mM TCEP, and 10% glycerol) supplemented with protease inhibitors (complete EDTA-free; Roche). Cell suspensions were lysed via five freeze-thaw cycles with liquid nitrogen and clarified via centrifugation at 15,000 rpm for 30 min. Clarified cell lysates were passed over anti-FLAG M2 resin

(Sigma) via gravity flow. Resin was washed with three column volumes of lysis buffer and incubated overnight with lysis buffer supplemented with 2.5 mM ATP and 5 mM $MgCl_2$ to remove chaperone. Resin was subsequently washed with three column volumes of lysis buffer and ATG2A proteins eluted with lysis buffer containing 0.2 µg/ml 3xFLAG peptide. E-Syt1, E-Syt2, and the tether-only construct were produced as previously described (Schauder et al., 2014; Bian et al., 2018).

Mass spectrometry

Full-length human ATG2A, expressed and purified as described above, was gel filtrated via a Superpose 6 Increase 10/30 column (GE Healthcare). Peak fractions were concentrated, and protein was quantified by Coomassie blue G250 staining using BSA standards. The sample was sent to Avanti Polar Lipids for lipid analysis, where bound lipids were extracted into a 1:1 (vol/vol) chloroform:methanol solution using a modified Bligh and Dyer extraction method. The sample was evaporated to dryness, then resuspended and diluted with an in-house standard containing phosphatidylcholine, PE, phosphatidylinositol, phosphatidylserine, phosphatidic acid, phosphatidylglycerol, sphingomyelin and phosphatidylglycerol, or sterol. For phospholipid analysis, sample was resolved on a 1.8-µm C8-column, and molecular species were detected with a Sciex 6500+ tandem mass spectrometer. For cholesterol analysis, sample was resolved on a 2.6-µm C18 column, and molecular species detected with a Sciex 5500 QTrap mass spectrometer. Lipids above an 8:1 signal-to-noise threshold were quantified and summed according to lipid class.

Native gel assays

Purified E-Syt2 at indicated concentrations was mixed with NBD-PS (0.5 mM final concentration) in 10-µl total reaction volumes and incubated on ice for 2 h to generate a standard curve for quantitating NBD-PS fluorescence. ATG2A protein was similarly incubated with NBD-labeled lipid. Samples were loaded onto 4–20% Mini-Protean Precast Native gels and run for 2 h at 100 V. NBD fluorescence was visualized using an ImageQuant LAS4000 (GE Healthcare). Then gels were stained with Coomassie blue G250 to visualize total protein. Images were analyzed via ImageJ (National Institutes of Health).

Cryo-EM sample preparation, data collection, and image processing

Samples were frozen using Vitrobot Mark IV (FEI) set at 4°C and 90% humidity. 4 µl of sample (0.075 mg/ml) was applied to a glow-discharged Quantifoil R 1.2/1.3 Au 400 grid. After 5-s wait time, grids were blotted for 3 s with a blot force of −2 and plunged into liquid ethane cooled to liquid nitrogen temperature.

Vitrified samples were imaged with a 300-kV Titan Krios electron microscope (Thermo Fisher Scientific) operated with SerialEM (Mastronarde, 2005) using a K2 Summit direct electron detector camera in superresolution counting mode. Data were recorded at a nominal magnification of 22,500× (calibrated pixel size of 1.3 Å) and a defocus range of −2.5 to −3.5 µm. A total exposure time of 10 s was dose-fractionated into 40 frames (250-ms exposure per frame), with a dose rate of 8 electrons/pixel/s (~1.18 electrons/Å^2/frame).

The 802 images were motion-corrected, dose-weighted, and binned over 2 × 2 pixels in MotionCor2 (Zheng et al., 2017b). The CTF was estimated using CTFFIND-4.1 (Rohou and Grigorieff, 2015). Poor-quality images (e.g., bad CTF fit, blurriness, ice contamination) were removed from the dataset. Particles were first automatically picked without templates in Gautomatch (http://www.mrc-lmb.cam.ac.uk/kzhang/Gautomatch/). The ~150,000 picked particles were extracted into 220 × 220-pixel boxes using Relion 2.0 (Kimanius et al., 2016), which was used for all following image-processing steps, and subjected to 2D classification (Fig. S1). Four of the resulting class averages were selected as templates for repicking in Gautomatch. The resulting 248,086 particles were subjected to 2D classification, and classes showing poor averages (ice contamination, poor structural features) were removed from the dataset. Based on the remaining class averages, an initial 3D model was generated, which was used for 3D refinement of the entire dataset, yielding a final density map at 15-Å resolution using gold-standard Fourier-shell correlation (FSC) and the FSC = 0.143 criterion. Several 3D classification schemes with and without masking were tested, but none yielded a substantially higher-resolution density map.

Liposome preparation

Liposomes for transfer assays were prepared as in Kumar et al. (2018). Briefly, lipids in chloroform were mixed in the indicated ratios; dried to thin films; reconstituted at a total lipid concentration of 1 mM in buffer containing 50 mM Hepes, pH 8.0, 500 mM NaCl, and 1 mM TCEP; and subjected to 10 freeze–thaw cycles. The liposomes were then freshly extruded 21 times through a polycarbonate filter with 100-nm pore size.

FRET-based lipid-transfer assay

Lipid-transfer experiments were set up at 30°C in 96-well plates, with 100-µl reaction volumes containing donor liposomes (200 µM final total lipid concentration: 61% DOPC, 30% liver PE, 2% NBD-PS, 2% Rh-PE, and 5% DGS-NTA [Ni]) and acceptor liposomes (200 µM total lipid: 65% DOPC, 30% liver PE, and 5% $PI(4,5)P_2$). Proteins (0.25 µM each of tether and lipid transport protein for a 1:800 protein:lipid ratio) were added to start the reaction, and after excitation at 460 nm, NBD emission (538 nm) was monitored for 2 h using a FlexStation 3 Multi-Mode Microplate Reader (Molecular Devices). All data were baseline corrected.

Dithionite assay

Lipid transfer assays were performed as above, except for the addition of freshly prepared dithionite (to 5-mM final concentration) after the last time point, and NBD fluorescence was monitored for an additional 30 min.

Cell culture

HEK293, HEK293FT, and Cos-7 cells were cultured in DMEM (Thermo Fisher Scientific; 11965092) supplemented with 10% FBS (Thermo Fisher Scientific; 10438062) and 1% penicillin-streptomycin (Thermo Fisher Scientific; 15140122) at 37°C in a 5% CO_2 incubator. For starvation experiments, cells were incubated in Earle's balanced salt solution (Thermo Fisher Scientific; 24010043) for 2 h.

Generation of *ATG2A/2B* DKO cell line by CRISPR/Cas9

CRISPR guide RNAs (gRNAs) targeting the first exons of ATG2A and ATG2B were designed using the online CRISPR Design Tool (Massachusetts Institute of Technology; http://tools.genome-engineering.org). The target sequences were ATG2A, 5′- CGC TGCCCTTGTACAGATCG-3′, and ATG2B, 5′-ATGGACTCCGAA AACGGCCA-3′. They were cloned into pX459 (Addgene; 62988) as described previously (Ran et al., 2013). HEK293 cells were transiently transfected with the constructs containing gRNAs and, after 48 h, were selected in 5 µg/ml puromycin for 1 d and seeded in 96-well plates for single clones. The clones were validated by genotyping and Western blotting. For genotyping, briefly, genomic DNAs from single clones were extracted using QuickExtract DNA extraction solution (Lucigen; QE0905T), and PCR products containing the site of Cas9 cleavage site were generated using the following primers: ATG2A-fw, 5′-AGCGGC CGCTTGAGAGCCCTATATCATGCAG-3′; ATG2A-rv, 5′-AGGATC CCTGGCTCTGGTAAGGAACTGAAGA-3′; ATG2B-fw, 5′-AGCGGC CGCTCGCGGATGACAACAAATTCG-3′; and ATG2B-rv, 5′-AGG ATCCGCAGCTCTTACCCATTTGTCCAA-3′. PCR products were gel purified and cloned into a plasmid, and single colonies were picked for plasmid preparation and sequencing.

Lentivirus production and transduction

HEK293FT cells (Thermo Fisher Scientific; R70007) were seeded into a 10-cm plate and grown to ∼60–70% confluence. Cells were then transfected with psPAX2 (Addgene; 12260), pCMV-VSV-G (Addgene; 8454), and target plasmid using Lipofectamine 3000 according to the manufacturer's suggestion. Cell medium was then collected every 24 h for 3 d and filtered with a 0.45-µm syringe filter (Pall; 4184). Lenti-X Concentrator (Clontech; 631231) was added at a ratio of 1:3, mixed with the filtrate by gentle inversion several times, and stored at 4°C for at least 2 h. The mixture was centrifuged at 1,500 *g* for 45 min at 4°C, and supernatant was carefully removed. The pellet was gently re-suspended in complete medium, aliquoted, and stored at −80°C for future use. One vial of lentivirus was used with polybrene to transduce target cell lines, and after 48 h, treated with 5 µg/ml puromycin and under selection for at least 1 wk.

Lysis, gel electrophoresis, and immunoblotting

Cells were washed once with ice-cold PBS, centrifuged at 800 *g* for 5 min at 4°C, and lysed in lysis buffer (10 mM Hepes, pH 7.5, 300 mM NaCl, and 0.2% Triton X-100) with EDTA-free protease inhibitor cocktail (Sigma; 11873580001) on ice. Lysates were collected after centrifugation at 20,000 *g* for 10 min at 4°C. Total protein concentration was determined by a BCA assay (Thermo Fisher Scientific; 23225). Samples were electrophoresed on precast Bis-Tris gels. Bolt 8% Bis-Tris Plus precast gels (Thermo Fisher Scientific; NW00082BOX) were used for anti-ATG2 and anti-GFP blots, while 12% Bis-Tris precast gels (Thermo Fisher Scientific; NP0341BOX or NP0342BOX) were used for all other targets. Gels were subsequently transferred to Immobilon-FL PVDF membranes (Sigma; IPFL00010) at 200 mA (for anti-ATG2 blot) or 30 V (for other targets) for 90 min.

Immunoblotting against LC3B and GABARAPL1 was described previously (Kauffman et al., 2018). For immunoblotting against all other proteins, membranes were rinsed in PBS, blocked with 1% casein (Sigma; C7078) in PBS with 0.2% sodium azide (Sigma; S2002) for 1 h at room temperature, rinsed in PBS-T (PBS containing 0.02% Tween 20 [AmericanBio; AB02038]), and incubated with primary antibody (diluted 1:1,000 in PBS-T containing 5% BSA [Sigma; A9647] and 0.005% sodium azide) overnight at 4°C. Membranes were washed three times in PBS-T before incubation with the IRDye secondary antibody (Li-COR; 925-68072 or 925-32213; diluted 1:10,000 in PBS containing 0.5% casein, 0.1% sodium azide, 0.1% SDS, and 0.25% Tween 20) for 1 h. Membranes were then washed three times in PBS-T and scanned with the Li-COR Odyssey system.

Protease protection assay

Cells were grown in 15-cm dishes until >90% confluence and treated with or without 100 nM bafilomycin A1 for 4 h. Cells were then washed with ice-cold PBS, centrifuged at 800 *g* for 5 min at 4°C, resuspended in 400 µl homogenization buffer (10 mM Hepes, pH 7.5, 0.22 M mannitol, and 0.07 M sucrose) with EDTA-free protease inhibitor cocktail (Sigma; 11873580001), and lysed with 2 ml Dounce homogenizer. Lysates were first centrifuged at 300 *g* for 5 min at 4°C. Postnuclear supernatants were further spun at 7,700 *g* for 5 min at 4°C. Pellets were saved as a low-speed pellet (LSP), while supernatants were further centrifuged in a TLA100.3 rotor (Beckman) operating at ∼100,000 *g* for 30 min at 4°C. The high-speed pellet (HSP) and high speed supernatant were collected. Both LSP and HSP were resuspended in 40 µl homogenization buffer. For each protease protection assay, an equal protein amount of each sample was incubated alone, with 5 µg/ml proteinase K (Roche; 03115887001), or with 5 µg/ml proteinase K and 0.5% Triton X-100 on ice for 30 min. Samples were boiled for 10 min to stop the reactions and subjected to SDS-PAGE and immunoblotting.

Western blot densitometry and quantification

Images of blots were evaluated in ImageStudioLite (Li-COR). For comparisons of LC3B-II (Fig. S2 E), the density for LC3B-II and p62 bands were first normalized against the GAPDH loading control. The normalized density of protein in cells rescued with full-length GFP-ATG2A (first lane in Fig. S2 E) set as 1. The relative ratio of LC3B-II in all other lanes is plotted as the ratio against this normalized value. For measurements of protease protection (Fig. S2 K), the total density of LC3B-II or p62 was measured in samples exposed to protease and divided by the total density of the same bands in samples without protease. Statistical significance was determined by two-way ANOVA. For comparison of p62 in Fig. S2 (H and J), the density for p62 bands at complete media conditions were normalized against the GAPDH loading control. Statistical significance was determined by unpaired *t* tests. All data are $n = 3$, plotted with mean ± SD in Prism 7 (GraphPad). Asterisks indicate significance determined by a two-way ANOVA; *, $P < 0.05$; **, $P < 0.01$; ***, $P < 0.001$; and ****, $P < 0.0001$.

IF

Cells seeded on poly-D-lysine–coated coverslips cells were rinsed in PBS, fixed in 4% PFA (Electron Microscopy Sciences; 15710), washed three times with PBS, quenched in 50 mM NH_4Cl, and

permeabilized in PBS containing 0.1% Triton X-100 (PBX). Incubation with primary or secondary antibody was done at room temperature for 1 h at indicated concentrations (see Reagents). After each incubation, cells were washed three times in PBX and mounted on precleaned microscope slides with ProLong Gold antifade reagent (Thermo Fisher Scientific; P36934). For experiments using anti-LC3B antibody, conditions were the same as above except cells were permeabilized and washed in PBS with 0.05% saponin (Sigma; 47036).

Antibody clearing

For endogenous ATG2A IF, anti-ATG2A antibody was first cleared as follows. *ATG2* DKO HEK293 cells were fixed in 4% PFA for 15 min, rinsed with PBS, quenched in 50 mM NH_4Cl in PBS, washed twice with PBS, permeabilized with PBX for 10 min, and scraped in PBX with 1% Triton X-100. Antibodies were added to the fixed cells at the final concentration used for IF (1:100) and mixed by rotation overnight at 4°C. The mixture was then centrifuged at 17,000 *g* for 20 min at 4°C, and the supernatant containing cleared antibodies was used for IF.

Confocal microscopy

At the Center for Cellular and Molecular Imaging Facility at Yale, imaging was performed with a 63× oil-immersion objective on an inverted Zeiss LSM 710 Duo NLO laser scanning confocal microscope or an inverted Zeiss LSM 880 laser scanning confocal microscope with AiryScan, using Zen acquisition software. Both have a 63× oil-immersion objective lens with NA = 1.4. Detection on the 710 is via photo multiplier tubes and a 34-channel quasar detector. The Airyscan detector is comprised of 32 GaAsP detectors. Images obtained with AiryScan were first processed using Airyscan Processing in Zen, and all images were analyzed in ImageJ.

Live imaging

Cells were seeded in poly-D-lysine–coated MatTek dishes (P35GC-1.5-14-C) and transfected with desired plasmids the next day. After 1 d, cells were treated with OA for 3–4 h (when analyzing GFP-ATG2A) and starved in live cell imaging solution (Thermo Fisher Scientific; A14291DJ) supplemented with 5 mM glucose for 1 h and imaged in the same solution at 37°C. For LD labeling, cells were washed with PBS, incubated with BODIPY 558/568 C_{12} (Thermo Fisher Scientific; D3835) for 1 h, washed with PBS, and subjected to further live-cell imaging or IF.

Online supplemental material

Fig. S1 shows cryo-EM reconstruction of human ATG2A. Fig. S2 shows rescue of autophagy phenotypes by GFP-ATG2A$_{1–345}$. Fig. S3 shows localization of GFP-ATG2A and endogenous ATG2A to autophagosomes.

Acknowledgments

We are deeply grateful to our colleague P. De Camilli for discussions regarding this manuscript, and to him, M. Leonzino, and W. Hancock-Cerutti for advice regarding imaging and immunostaining.

This work was supported by grants from the National Institutes of Health (GM1000930 and NS063973 to T.J. Melia; GM080616 and GM114068 to K.M. Reinisch), predoctoral training grants from the China Scholarship Council to S. Yu and from the National Institutes of Health to D.P. Valverde (T32 GM007223), and a National Science Foundation Graduate Research Fellowship to D.P. Valverde.

The authors declare no competing financial interests.

Author contributions: D.P. Valverde designed and carried out all the biochemical assays for lipid binding and transfer by full-length and mini-ATG2 constructs, with input from N. Kumar and J.A. Lees, and prepared full-length ATG2 for cryo-EM analysis. S. Yu designed and performed all the cell biology experiments. V. Boggavarapu determined the single-particle reconstruction of ATG2. T.J. Melia and K.M. Reinisch designed the project and supervised it with T. Walz. The manuscript was prepared by T.J. Melia and K.M. Reinisch with help from T. Walz, S. Yu, and D.P. Valverde.

Submitted: 26 November 2018
Revised: 5 March 2019
Accepted: 28 March 2019

References

Axe, E.L., S.A. Walker, M. Manifava, P. Chandra, H.L. Roderick, A. Habermann, G. Griffiths, and N.T. Ktistakis. 2008. Autophagosome formation from membrane compartments enriched in phosphatidylinositol 3-phosphate and dynamically connected to the endoplasmic reticulum. *J. Cell Biol.* 182:685–701. https://doi.org/10.1083/jcb.200803137

Bian, X., Y. Saheki, and P. De Camilli. 2018. Ca^{2+} releases E-Syt1 autoinhibition to couple ER-plasma membrane tethering with lipid transport. *EMBO J.* 37:219–234. https://doi.org/10.15252/embj.201797359

Chowdhury, S., C. Otomo, A. Leitner, K. Ohashi, R. Aebersold, G.C. Lander, and T. Otomo. 2018. Insights into autophagosome biogenesis from structural and biochemical analyses of the ATG2A-WIPI4 complex. *Proc. Natl. Acad. Sci. USA.* 115:9792–9801. https://doi.org/10.1073/pnas.1811874115

Fang, X.T., D. Sehlin, L. Lannfelt, S. Syvänen, and G. Hultqvist. 2017. Efficient and inexpensive transient expression of multispecific multivalent antibodies in Expi293 cells. *Biol. Proced. Online.* 19:11. https://doi.org/10.1186/s12575-017-0060-7

Gómez-Sánchez, R., J. Rose, R. Guimarães, M. Mari, D. Papinski, E. Rieter, W.J. Geerts, R. Hardenberg, C. Kraft, C. Ungermann, and F. Reggiori. 2018. Atg9 establishes Atg2-dependent contact sites between the endoplasmic reticulum and phagophores. *J. Cell Biol.* 217:2743–2763. https://doi.org/10.1083/jcb.201710116

Hamasaki, M., N. Furuta, A. Matsuda, A. Nezu, A. Yamamoto, N. Fujita, H. Oomori, T. Noda, T. Haraguchi, Y. Hiraoka, et al. 2013. Autophagosomes form at ER-mitochondria contact sites. *Nature.* 495:389–393. https://doi.org/10.1038/nature11910

Harding, T.M., K.A. Morano, S.V. Scott, and D.J. Klionsky. 1995. Isolation and characterization of yeast mutants in the cytoplasm to vacuole protein targeting pathway. *J. Cell Biol.* 131:591–602. https://doi.org/10.1083/jcb.131.3.591

Hurley, J.H., and L.N. Young. 2017. Mechanisms of Autophagy Initiation. *Annu. Rev. Biochem.* 86:225–244. https://doi.org/10.1146/annurev-biochem-061516-044820

Kauffman, K.J., S. Yu, J. Jin, B. Mugo, N. Nguyen, A. O'Brien, S. Nag, A.H. Lystad, and T.J. Melia. 2018. Delipidation of mammalian Atg8-family proteins by each of the four ATG4 proteases. *Autophagy.* 14:992–1010.

Kimanius, D., B.O. Forsberg, S.H. Scheres, and E. Lindahl. 2016. Accelerated cryo-EM structure determination with parallelisation using GPUs in RELION-2. *eLife.* 5:e18722. https://doi.org/10.7554/eLife.18722

Kotani, T., H. Kirisako, M. Koizumi, Y. Ohsumi, and H. Nakatogawa. 2018. The Atg2-Atg18 complex tethers pre-autophagosomal membranes to the endoplasmic reticulum for autophagosome formation. *Proc. Natl. Acad. Sci. USA.* 115:10363–10368. https://doi.org/10.1073/pnas.1806727115

Kumar, N., M. Leonzino, W. Hancock-Cerutti, F.A. Horenkamp, P. Li, J.A. Lees, H. Wheeler, K.M. Reinisch, and P. De Camilli. 2018. VPS13A and

VPS13C are lipid transport proteins differentially localized at ER contact sites. *J. Cell Biol.* 217:3625–3639. https://doi.org/10.1083/jcb.201807019

Lees, J.A., M. Messa, E.W. Sun, H. Wheeler, F. Torta, M.R. Wenk, P. De Camilli, and K.M. Reinisch. 2017. Lipid transport by TMEM24 at ER-plasma membrane contacts regulates pulsatile insulin secretion. *Science.* https://doi.org/10.1126/science.aah6171.

Longo, P.A., J.M. Kavran, M.S. Kim, and D.J. Leahy. 2013. Transient mammalian cell transfection with polyethylenimine (PEI). *Methods Enzymol.* 529:227–240. https://doi.org/10.1016/B978-0-12-418687-3.00018-5

Maeda, K., K. Anand, A. Chiapparino, A. Kumar, M. Poletto, M. Kaksonen, and A.C. Gavin. 2013. Interactome map uncovers phosphatidylserine transport by oxysterol-binding proteins. *Nature.* 501:257–261. https://doi.org/10.1038/nature12430

Mastronarde, D.N. 2005. Automated electron microscope tomography using robust prediction of specimen movements. *J. Struct. Biol.* 152:36–51. https://doi.org/10.1016/j.jsb.2005.07.007

Meers, P., S. Ali, R. Erukulla, and A.S. Janoff. 2000. Novel inner monolayer fusion assays reveal differential monolayer mixing associated with cation-dependent membrane fusion. *Biochim. Biophys. Acta.* 1467: 227–243. https://doi.org/10.1016/S0005-2736(00)00224-8

Molino, D., N. Zemirli, P. Codogno, and E. Morel. 2017. The Journey of the Autophagosome through Mammalian Cell Organelles and Membranes. *J. Mol. Biol.* 429:497–514. https://doi.org/10.1016/j.jmb.2016.12.013

Muñoz-Braceras, S., R. Calvo, and R. Escalante. 2015. TipC and the chorea-acanthocytosis protein VPS13A regulate autophagy in Dictyostelium and human HeLa cells. *Autophagy.* 11:918–927. https://doi.org/10.1080/15548627.2015.1034413

Pfisterer, S.G., D. Bakula, A. Cezanne, H. Robenek, and T. Proikas-Cezanne. 2014a. WIPI β-propellers at the crossroads of autophagosome and lipid droplet dynamics. *Biochem. Soc. Trans.* 42:1414–1417. https://doi.org/10.1042/BST20140152

Pfisterer, S.G., D. Bakula, T. Frickey, A. Cezanne, D. Brigger, M.P. Tschan, H. Robenek, and T. Proikas-Cezanne. 2014b. Lipid droplet and early autophagosomal membrane targeting of Atg2A and Atg14L in human tumor cells. *J. Lipid Res.* 55:1267–1278. https://doi.org/10.1194/jlr.M046359

Ran, F.A., P.D. Hsu, J. Wright, V. Agarwala, D.A. Scott, and F. Zhang. 2013. Genome engineering using the CRISPR-Cas9 system. *Nat. Protoc.* 8: 2281–2308. https://doi.org/10.1038/nprot.2013.143

Rohou, A., and N. Grigorieff. 2015. CTFFIND4: Fast and accurate defocus estimation from electron micrographs. *J. Struct. Biol.* 192:216–221. https://doi.org/10.1016/j.jsb.2015.08.008

Saheki, Y., X. Bian, C.M. Schauder, Y. Sawaki, M.A. Surma, C. Klose, F. Pincet, K.M. Reinisch, and P. De Camilli. 2016. Control of plasma membrane lipid homeostasis by the extended synaptotagmins. *Nat. Cell Biol.* 18: 504–515. https://doi.org/10.1038/ncb3339

Schauder, C.M., X. Wu, Y. Saheki, P. Narayanaswamy, F. Torta, M.R. Wenk, P. De Camilli, and K.M. Reinisch. 2014. Structure of a lipid-bound extended synaptotagmin indicates a role in lipid transfer. *Nature.* 510: 552–555. https://doi.org/10.1038/nature13269

Suzuki, K., M. Akioka, C. Kondo-Kakuta, H. Yamamoto, and Y. Ohsumi. 2013. Fine mapping of autophagy-related proteins during autophagosome formation in Saccharomyces cerevisiae. *J. Cell Sci.* 126:2534–2544. https://doi.org/10.1242/jcs.122960

Tamura, N., T. Nishimura, Y. Sakamaki, I. Koyama-Honda, H. Yamamoto, and N. Mizushima. 2017. Differential requirement for ATG2A domains for localization to autophagic membranes and lipid droplets. *FEBS Lett.* 591:3819–3830. https://doi.org/10.1002/1873-3468.12901

Tang, Z., Y. Takahashi, C. Chen, Y. Liu, H. He, N. Tsotakos, J.M. Serfass, M.T. Gebru, H. Chen, M.M. Young, and H.G. Wang. 2017. Atg2A/B deficiency switches cytoprotective autophagy to non-canonical caspase-8 activation and apoptosis. *Cell Death Differ.* 24:2127–2138. https://doi.org/10.1038/cdd.2017.133

Tsukada, M., and Y. Ohsumi. 1993. Isolation and characterization of autophagy-defective mutants of Saccharomyces cerevisiae. *FEBS Lett.* 333:169–174. https://doi.org/10.1016/0014-5793(93)80398-E

Velikkakath, A.K., T. Nishimura, E. Oita, N. Ishihara, and N. Mizushima. 2012. Mammalian Atg2 proteins are essential for autophagosome formation and important for regulation of size and distribution of lipid droplets. *Mol. Biol. Cell.* 23:896–909. https://doi.org/10.1091/mbc.e11-09-0785

Yu, H., Y. Liu, D.R. Gulbranson, A. Paine, S.S. Rathore, and J. Shen. 2016. Extended synaptotagmins are Ca2+-dependent lipid transfer proteins at membrane contact sites. *Proc. Natl. Acad. Sci. USA.* 113:4362–4367. https://doi.org/10.1073/pnas.1517259113

Zhao, Y.G., Y. Chen, G. Miao, H. Zhao, W. Qu, D. Li, Z. Wang, N. Liu, L. Li, S. Chen, et al. 2017. The ER-Localized Transmembrane Protein EPG-3/VMP1 Regulates SERCA Activity to Control ER-Isolation Membrane Contacts for Autophagosome Formation. *Mol. Cell.* 67:974–989.e6. https://doi.org/10.1016/j.molcel.2017.08.005

Zhao, Y.G., N. Liu, G. Miao, Y. Chen, H. Zhao, and H. Zhang. 2018. The ER Contact Proteins VAPA/B Interact with Multiple Autophagy Proteins to Modulate Autophagosome Biogenesis. *Curr. Biol.* 28:1234–1245.e4. https://doi.org/10.1016/j.cub.2018.03.002

Zheng, J.X., Y. Li, Y.H. Ding, J.J. Liu, M.J. Zhang, M.Q. Dong, H.W. Wang, and L. Yu. 2017a. Architecture of the ATG2B-WDR45 complex and an aromatic Y/HF motif crucial for complex formation. *Autophagy.* 13: 1870–1883. https://doi.org/10.1080/15548627.2017.1359381

Zheng, S.Q., E. Palovcak, J.P. Armache, K.A. Verba, Y. Cheng, and D.A. Agard. 2017b. MotionCor2: anisotropic correction of beam-induced motion for improved cryo-electron microscopy. *Nat. Methods.* 14:331–332. https://doi.org/10.1038/nmeth.4193